

Imaging concrete cracks using Nonlinear Coda Wave Interferometry (INCWI)

Shilin Qu^a, Benoît Hilloulin^{b,*}, Jacqueline Saliba^c, Mehdi Sbartaï^c, Odile Abraham^a, Vincent Tournat^d

^a GERS-GeoEND, Univ Gustave Eiffel, IFSTTAR, CS5004, F-44344 Bouguenais, France

^b Nantes Université, Ecole Centrale Nantes, CNRS, GeM, UMR 6183, F-44000 Nantes, France

^c I2M, UMR 5295, University of Bordeaux, Talence, France

^d Laboratoire d'Acoustique de l'Université du Mans (LAUM), UMR 6613, Institut d'Acoustique - Graduate School (IA-GS), CNRS, Le Mans Université, France

ARTICLE INFO

Keywords:

Concrete
Coda
Nonlinear acoustics
Crack breathing
Ultrasound
Acoustic emission
NCWI

ABSTRACT

Crack imaging in highly heterogeneous materials, such as concrete, plays a great role in structural health monitoring and non-destructive evaluation and testing. Numerous works have shown that Nonlinear Coda Wave Interferometry is a robust tool to assess the overall level of nonlinearity caused by micro or macrocracks in heterogeneous media. This work presents a novel qualitative method for Imaging using NCWI (INCWI) based on the combination of Nonlinear Coda Wave Interferometry (NCWI) and a spatial averaging method. INCWI is used herein to locate cracks generated in a concrete beam subject to three-point bending. Measurements are performed after each loading level, in both pre-peak and post-peak phases, once the beam has been unloaded. The imaging algorithm is described and applied to each stage of beam damage. In the post-peak phase, crack size varies from 10 cm to 15 cm in length and from 25 μm to 200 μm in width. Also, the INCWI results are compared with acoustic emission measurements and microscopic observations.

1. Introduction

Cracks can appear at the microscopic or macroscopic scales in various types of concrete, ranging from ordinary Portland cement (OPC) concrete to Ultra-high performance Fiber Reinforced Concrete (UHPFRC). Several causes can be highlighted, including early-age or long-term shrinkage [1–3], chemical degradations [4,5] and the creep mechanism [6,7]. Since cracks in structures can be dangerous and considerably decrease their durability, developing techniques for crack detection and localization in concrete proves to be very important.

Numerous non-destructive testing and evaluation (NDT&E) ultrasonic techniques have been devised for crack detection and localization. For example, among the most widely applied linear techniques, Acoustic Emission (AE) [8–12] is able to localize the Fracture Process Zone (FPZ) and quantify the intensity of acoustic events related to crack friction or crack propagation during the fracture process. Moreover, Ultrasonic Pulse Velocity (UPV) [13–16] helps assess the quality of inspected beams by means of measuring of the travel time of ultrasonic body waves. Other linear methods using surface waves can also characterize cracks in concrete [17–19]. However, these techniques can encounter practical difficulties depending on the purpose of inspection. For instance, AE must be performed when an external load is being applied, and the arrival time in a UPV test can be both challenging to estimate and operator-dependent for microcracks or partially closed

cracks due to the lack of impedance contrast between the cracked and uncracked areas. On the other hand, methods based on surface waves can sometimes be limited by penetration depth as well as by partially closed cracks. Therefore, developing sensitive yet easy-to-implement techniques capable of circumventing these drawbacks is of great interest for long-term and large-scale monitoring campaigns.

Recent studies on wave/crack interactions have revealed that when the amplitude of acoustic excitation over a closed crack is high enough, a hysteretic nonlinear interaction between acoustic waves and the crack can occur, whereby the crack tips alternate between open and closed states. This phenomenon is known as crack breathing [20–23]. Both numerical [24–26] and experimental [25,27] studies have been carried out in order to demonstrate the relevant nonlinear signatures, such as nonlinear harmonics and hysteresis. Crack breathing provides multiple nonlinear parameters, which have been used as nonlinearity level indicators in numerous works on crack imaging with nonlinear ultrasound. For example, in [28,29], stretching parameters and parameters related to the harmonic generation due to contact and frictional behavior at the crack tip were used in combination with a time reversal mirror to locally probe and image the nonlinearity of a cracked region. In [30], the group velocity variation caused by the interaction between crack breathing and nonlinear Lamb waves was

* Corresponding author.

E-mail addresses: shilin.qu@univ-eiffel.fr (S. Qu), benoit.hilloulin@ec-nantes.fr (B. Hilloulin), odile.abraham@univ-eiffel.fr (O. Abraham).

applied with an imperfect group velocity matching of nonlinear S_0 modes in order to detect and image microstructural changes. Despite their accuracy of crack localization, these methods can be limited by depth, structural type and frequency. The frequency limitation stems from the need for specific frequencies of nonlinear S_0 modes. As for structural and depth limitations, the time reversal method [28] requires the defect to be surface-breaking or at least near the surface. To localize defects inside a structure, an accurate numerical model is needed to numerically calculate the corresponding re-broadcasted time reversal signal, which can be computationally cumbersome. The nonlinear Lamb mode method [30], on the other hand, is limited by a homogeneous plate-like structure as well as by the frequency of nonlinear S_0 modes. Therefore, an imaging method with less of the limitations mentioned above would be desirable.

Furthermore, crack detection and localization using acoustic waves can prove to be challenging in highly heterogeneous media due to strong scattering, which can render the ballistic acoustic wave ineffective. Over the past two decades, coda waves, a type of multiple scattered elastic waves, have shown various advantages in defect detection and localization in heterogeneous elastic media thanks to their high sensitivity to small changes. This type of wave has been used in the Coda Wave Interferometry (CWI) technique as a basic principle of crack detection/imaging techniques [31,32], however, the need for a crack state variation is one of its major limitations since such a situation cannot be encountered under various onsite scenarios. Low-frequency pump wave excitation has thus been introduced to overcome this drawback in the Nonlinear Coda Wave Interferometry (NCWI) technique, thus inducing a crack breathing phenomenon. Recent works on NCWI have demonstrated its high sensitivity to material property changes and micro or macrocrack detection in both homogeneous and heterogeneous materials, ranging in scale from laboratory [33–38] to large in situ [39]. Despite the inherent advantages of NCWI in crack detection, the use of NCWI to localize cracks still remains a challenge since no imaging technique based on NCWI has yet to be published.

Given this motivation, a novel imaging method is being sought that can overcome the need for applying an external load while ensuring a reasonable computational cost. A qualitative imaging technique using Nonlinear Coda Wave Interferometry (INCWI) to localize a three-point bending-generated crack is presented in this study. In order to localize the crack, multiple Source–Receiver (SR) sensor couples have been used during NCWI to measure NCWI parameters along various propagation trajectories. NCWI typical outputs, e.g., relative velocity variation (θ) and decorrelation coefficient (K_d), have been calculated for all S-R couples. A qualitative imaging can then be produced via a dedicated averaging method. To prove the robustness of this qualitative tomography technique, the NCWI process has been performed over multiple three-point bending load levels, involving for example various crack lengths, including both pre-peak and post-peak phases. Acoustic emissions and optical microscopy measurements have also been conducted to compare the method's crack localization capability.

2. Materials and analysis method

2.1. CWI and NCWI

In CWI, multiple scattered waves, denoted coda waves, are introduced to detect temporal changes in a medium, such as temperature fluctuation or fatigue cracking. The principle behind CWI consists of comparing coda signals in different material states. A sweep sine signal, whose wavelengths are comparable to the size of the heterogeneities, serves as a source of probe waves to generate the coda signals thanks to multiple scattering in the beam. A reference coda $u_i(t)$ is recorded at an initial state (i.e. the intact state), and a perturbed coda $u_p(t)$ is recorded at another state (i.e. the damaged state). The creation of microcracks leads to two major effects: (1) a local decrease in Young's modulus around the cracks, hence a small decrease in wave velocity; and (2)

Table 1

| Concrete composition kg/m ³ . | | | |
|--|------|-----------|------|
| Cement | Sand | Aggregate | w/c |
| 350 | 890 | 984 | 0.55 |

a modification in the scattering property of elastic waves. These two effects can be quantified by two CWI observables, namely θ and K_d . θ can be calculated according to the stretching method (Eq. (1)):

$$CC(\theta_n) = \frac{\int_{t_1}^{t_2} u_i(t(1 + \theta_n))u_p(t)dt}{\sqrt{\int_{t_1}^{t_2} u_i^2(t(1 + \theta_n))dt \int_{t_1}^{t_2} u_p^2(t)dt}}, \quad (1)$$

where $u_i(t)$ and $u_p(t)$ denote the reference and perturbed codas, respectively for travel times between t_1 and t_2 [40]. The final value of θ is the one that maximizes $CC(\theta_n)$ and K_d is calculated using the following equation:

$$K_d = 100(1 - CC(\theta)). \quad (2)$$

Based on CWI, the NCWI method has been developed by applying a nonlinear mix of low frequency (LF) sweep pump waves at varying amplitudes A_{pump} during the CWI process [37]. The inspected object is expected to be insonified evenly across space by the pump waves in order to eliminate the influence of spatial variation of pump wave amplitude. The nonlinear pump waves enable the activation of crack breathing for closed (or partially closed) cracks [41–43], which will further interact with the probe waves. This interaction will perturb the high frequency (HF) probe signals which can be quantified by two parameters: relative velocity change θ and waveform decorrelation coefficient K_d . θ can be calculated by means of the stretching method [44] which evaluates the time dilation of the perturbed coda waves at the point of reception compared to the reference coda waves (no pump wave). K_d can be calculated according to θ which provides the waveform difference between reference and perturbed coda waves. Both the θ , K_d pair and their variation rates versus pump wave amplitude α_θ , α_{K_d} make it possible to characterize the global nonlinearity level of the inspected beam due to the crack. θ and K_d are measured at different pump wave amplitudes and crack sizes, while α_θ and α_{K_d} are measured at different crack sizes.

2.2. Experimental design

2.2.1. Concrete beam preparation

A group of three 50 cm \times 25 cm \times 12 cm concrete beams was prepared using CEM I 52.5 N cement, 0/4 and 4/12 calcareous sand and aggregates, with a water-to-cement ratio of 0.55 (see Table 1). Three additional cylinders were also cast to measure the 28-day compressive strength. After 24 h of curing under sealed conditions in a room at 20 °C and 85–95% relative humidity, the specimens were demolded. The cylinders were cured in water until the age of 28 days. The beams were cured in water for 21 days and then subjected to air curing for another two weeks. The maximum compressive strength of the cylinders was measured on a hydraulic press according to NF EN 12390-3. According to the results, the average compressive strength could be estimated at approx. 42 MPa.

2.2.2. Three-point bending test protocol

The three-point bending test has been selected to generate a single crack in the concrete beams. The bending load bench and inspected beam are presented in Fig. 1(a). A hydraulic press (maximum load: 500 kN, precision: 0.1 kN) was used to apply a load on the upper central part of the inspected beam and the bottom supports were placed 20 cm apart from the center of the beam. A 5 mm \times 10 mm notch was made on the lower central part of the inspected beam (see Fig. 1(b)) to create

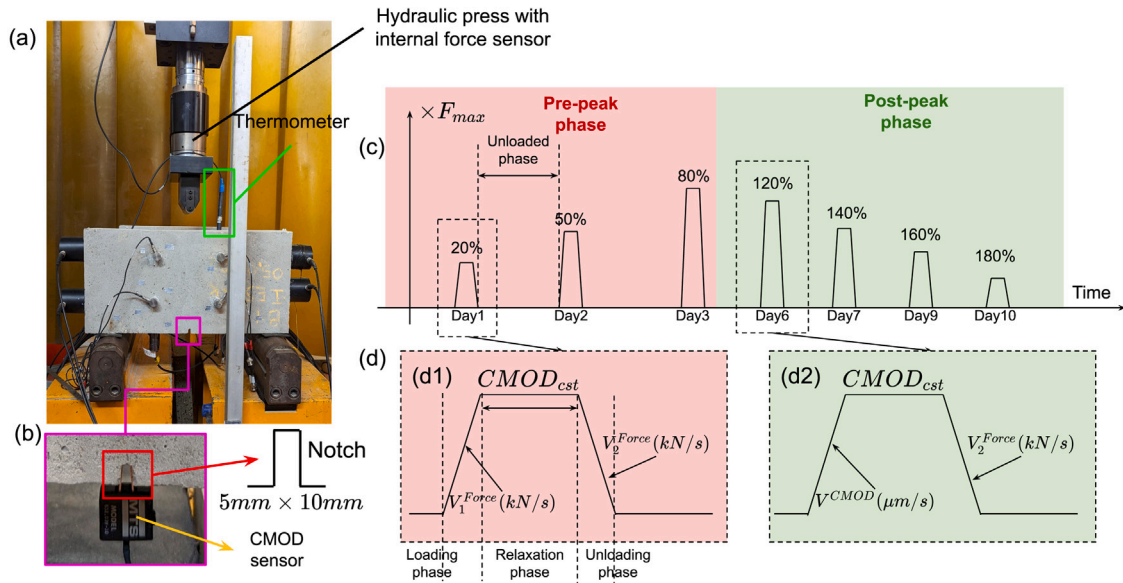


Fig. 1. Three-point bending set-up and protocol. (a), three-point bending load bench with the inspected beam (front face). (b), zoom on the notch ($5\text{ mm} \times 10\text{ mm}$) and the CMOD transducer at the lower center part of the inspected beam. (c), overall three-point bending load protocol. (d), detailed loading protocols of pre-peak phase (d1) and post-peak phase (d2).

a stress concentration and localize the crack generation. Over a 10-day period, the inspected beam was cyclically loaded at increasing load levels. At the same time, a reference beam (without the application of a static load) was mounted adjacent to the inspected beam in order to record environmental perturbations.

The three-point bending load protocol is divided into three pre-peak cycles and four post-peak cycles, with each phase containing multiple steps, as illustrated in Fig. 1(c). One loading cycle contains the four following steps, detailed in Fig. 1(d): (1) loading phase — the bending load or the CMOD (Crack Mouth Opening Displacement), measured at mid-span using a clip gauge, increases at a rate of 0.05 kN/s or $0.05\text{ }\mu\text{m/s}$ for the pre-peak or post-peak cycles respectively; (2) a relaxation phase: after reaching the expected amplitude of force or CMOD, the pilot force is adjusted during this phase so as to maintain the CMOD at a constant value; (3) an unloading phase: unloading at the speed of 0.05 kN/s and (4) an unloaded phase: free from all bending load to proceed with the INCWI measurements. The creep duration was intentionally decreased with an increase in bending load level in order to lower the risk of failure or excessive damage during this phase.

During the pre-peak phase, the test was load-controlled. The loading level was situated below the maximum flexural load measured beforehand on a reference companion beam measured beforehand $F_{max} = 40.5\text{ kN}$ ($20\%F_{max}$, $50\%F_{max}$ and $80\%F_{max}$ levels). Before entering the post-peak phase, the bending load level was increased from $80\%F_{max}$ to F_{max} . During the post peak phase, CMOD values were set based on the correspondence between load and CMOD for the companion beam. Once the target value of CMOD corresponding to $80\%F_{max}$, $60\%F_{max}$, $40\%F_{max}$ or $20\%F_{max}$ (denoted $120\%F_{max}$, $140\%F_{max}$, $160\%F_{max}$ and $180\%F_{max}$ resp.) was reached, CMOD had been maintained constant for a few minutes to allow for one single NCWI measurement as explained Section 2.3.2.

Recordings of the evolution in the actual CMOD at the notch vs. the loading force during the pre-peak and post-peak phases are shown in Fig. 2. Two remarks can be made based on these results: the behavior of the beam is nearly perfectly linear during the pre-peak phase with limited inelastic deformations; and the maximum bending load of the inspected beam, as measured during the fourth loading cycle, equals 41.7 kN , which is close to the maximum load measured on the companion beam.

2.3. INCWI methodology

2.3.1. CWI and NCWI set-up

The experimental set-up for CWI and NCWI is illustrated in Fig. 3: four piezoelectric transducers (shown in red) were mounted on both the left and right faces of the inspected beam to generate LF pump waves (two transducers on each side). The pump wave transducers on the left face were shifted compared to the right face in order to avoid interference. 10 source transducers (S) in orange and 14 receiver transducers (R) in green were mounted on the rear and bottom faces of the inspected beam; moreover, one source transducer and one receiver transducer were mounted on the rear face of the reference beam, with their locations corresponding to those of S3 and R10 on the inspected beam, in order to apply temperature-correction algorithms, as explained in [45].

In order to obtain more information on the micro or macrocrack generation during bending load, more transducers are glued at the lower half zone of the inspected beam where crack generations are likely to occur. It has been decided to adopt a similar distribution pattern as the one used in another study related to imaging using CWI [46]. Interestingly, such a pattern leads to many intersections between the S-to-R paths and the crack zone situated at the lower center of the beam. Although the INCWI technique would be applicable, the results' precision would decrease with a lower number of sensors. Future research and advanced optimization algorithms might help decrease the number of sensors for a given image quality. Two source-receiver couples were glued to the bottom face so as to detect material property changes with depth.

A schematic diagram of the ultrasound acquisition system of CWI and NCWI is shown in Fig. 4. Synthetic chirp waves were generated in burst mode from PC controller for both pump ($10\text{ kHz}–50\text{ kHz}$) and probe ($200\text{ kHz}–800\text{ kHz}$) waves, and amplified pump and probe waves were desynchronized to guarantee a random temporal distribution of HF probe wave packets over LF pump waves. The coda waves were filtered by a high-pass filter to eliminate the LF noise from the pump waves before recording.

The synthetic chirp signals of the pump and probe are illustrated in Fig. 5: one burst of the pump wave signal lasts 11 ms with a frequency range extending from 10 kHz to 50 kHz . One burst of the probe wave signal lasts 0.2 ms with a frequency range from 200 kHz to 800 kHz . This

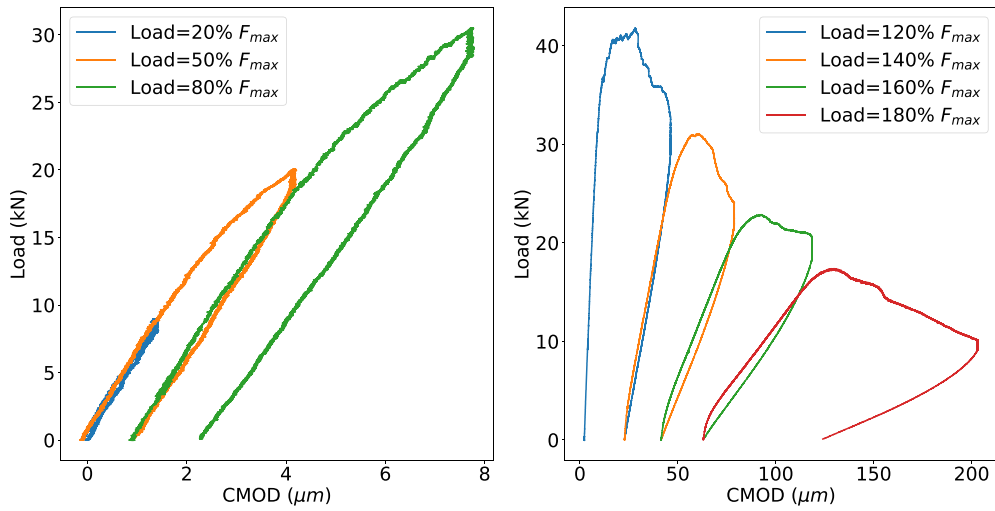


Fig. 2. Record of real CMOD at notch and loading force versus real CMOD during pre-peak phase.

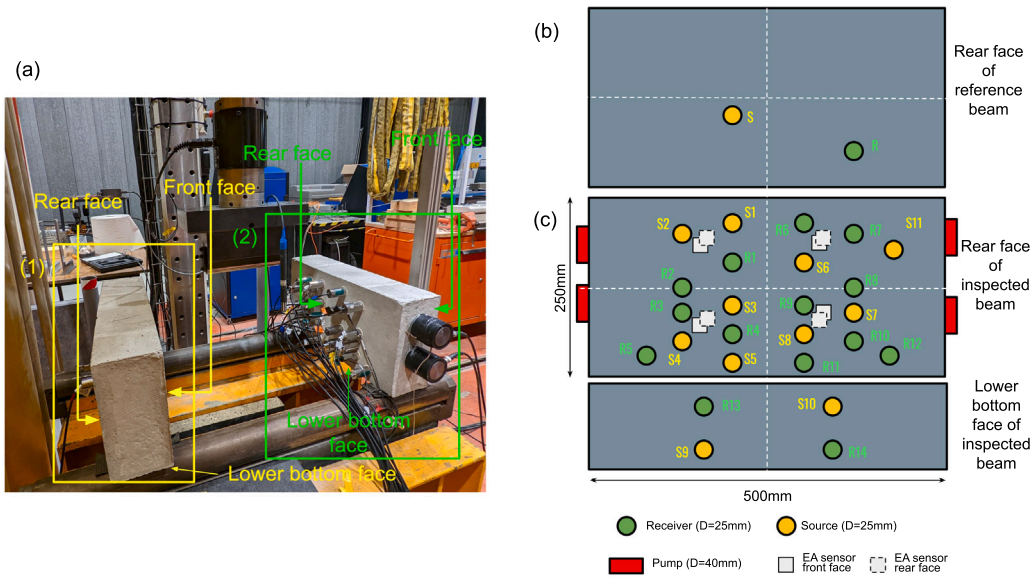


Fig. 3. (a) Photograph of the reference beam and the inspected beam. (b) position of sources and receivers on the reference beam. (c) position of transducers on the inspected beam. (For interpretation of the references to color in this figure legend, the reader is referred to the web version of this article.)

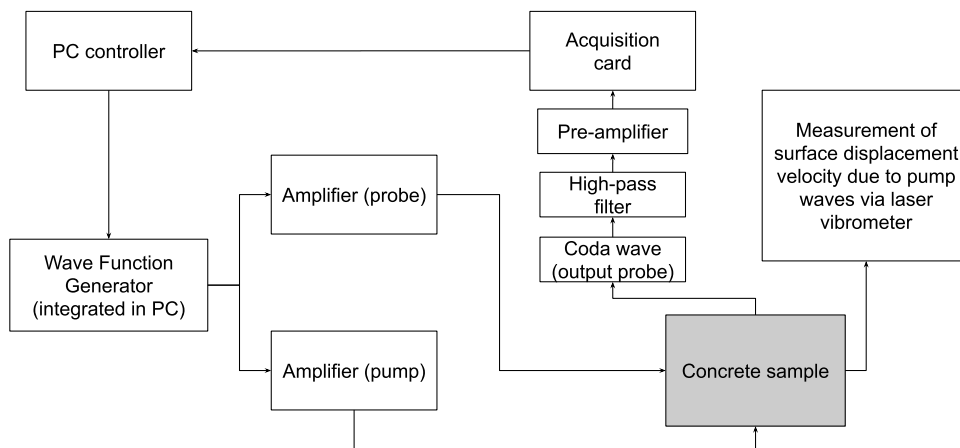


Fig. 4. Schematic diagram of the ultrasound acquisition system during the monitoring phase.

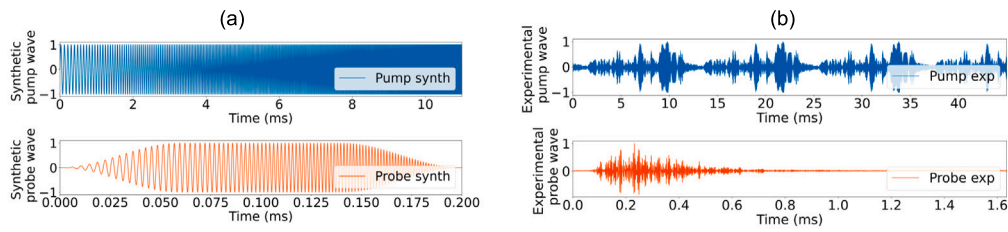


Fig. 5. Examples of source and received pump and probe signals. (a) synthetic pump and probe source signals. (b) received pump and probe signals at R7.

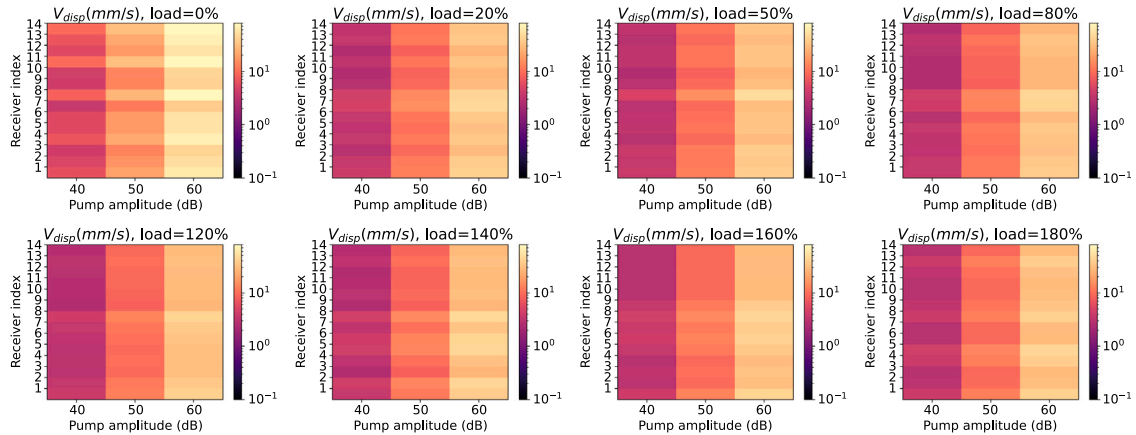


Fig. 6. Surface displacement velocity V_{disp} due to different pump waves amplitudes (40 dB, 50 dB, and 60 dB) at all receiver positions after static bending load applications at various levels.

pump wave frequency range was chosen in order to activate tens of fundamental modes of the inspected beam, to ensure a spatial equipartition of pump wave energy. The coda wave frequency band has been validated in previous publications [47]: it includes wavelengths of the order of the aggregate size to generate scattering and is compatible with an investigation distance of 24 cm to 35 cm. Examples of the received pump and probe signals are presented in Fig. 5(b). The acquisition time of the pump wave is four times the burst duration for the purpose of demonstrating the periodicity of the pump wave burst, moreover, the acquisition time of the probe wave is 1.6 ms, i.e. long enough to include the entire wave envelope from initiation to disappearance. Ultrasonic transducers were distributed over a 2D surface, while the pump wave amplitude is expected to be homogeneous in space throughout the NCWI measurement to eliminate all error from the spatial pump wave amplitude variation.

In order to verify the homogeneous spatial energy distribution of pump waves in the inspected beam, the spatial pump wave energy distribution was measured by recording the out-of-plane displacement velocity V_{disp} at all receiver positions by means of a laser vibrometer. V_{disp} was measured after each bending load at 3 pump wave amplitudes 40 dB, 50 dB, and 60 dB. The values of V_{disp} were chosen from the spectrum amplitude at the central frequency of the input pump waves (30 kHz). The V_{disp} results and standard deviation are presented in Figs. 6 and 7. The standard deviation against all receiver positions remains stable under 10% apart from no bending load case (0%). The standard deviation increases with the pump wave amplitude, likely due to the dependency of the scattering property on the pump wave amplitude.

2.3.2. CWI and NCWI protocol

CWI and NCWI are performed during each bending load cycle. An example of the timeline of a single measurement cycle is illustrated in Fig. 8, with each cycle lasting approximately one day. During a given cycle, the measurement is divided into the bending test phase and the monitoring phase, and during the monitoring phase, the concrete

beam is free of any bending load. Next, a series of measurements of the surface displacement velocity (V_{disp}) due to pump waves at all reception positions is conducted by means of a laser vibrometer. These measurements are used to assess the spatial energy distribution of the pump wave. Since the ideal case, calls for the concrete beam to be insonified evenly in space by the pump waves, the spatial energy distribution of pump waves is expected to be homogeneous at both all bending load levels as well as all pump waves amplitudes. After the laser measurement, CWI and NCWI are carried out consecutively, one followed by the other.

2.3.3. Qualitative imaging

In order to localize the crack thanks to the newly developed imaging technique, information from all source–receiver couples needs to be taken into account, similar to methods employed for the continuous damage detection in concrete during strong environmental variations [48,49]. In NCWI, it has been observed that θ and K_d vary linearly, resp. quadratically, relative to the pump amplitude, as expressed in Eqs. (3) and (4) [33,35,50]. The linear coefficient, resp. second order coefficient, is denoted α_θ , resp. α_{K_d} .

$$\theta = \alpha_\theta A_{pump}, \quad (3)$$

$$K_d = \alpha_{K_d} A_{pump}^2, \quad (4)$$

For the case herein, a qualitative imaging method using the spatial average of NCWI observables (α_θ and α_{K_d}) is being proposed, as described by Eq. (5): for a system containing N_{src} source transducers and N_{recp} receiver transducers, the 2D medium is discretized into a N_x by N_y grid, with grid elements being labeled by i (longitudinal location) and j (vertical location). Let us consider the source–receiver couple (S_p, R_q) that forms a line whose width equals the value of α_θ or α_{K_d} related to this (S_p, R_q) couple. If this (S_p, R_q) couple line passes through element (i,j), the intersection length can be calculated and denoted d_{ijpq} . Each rectangular element (i,j) may be crossed by multiple

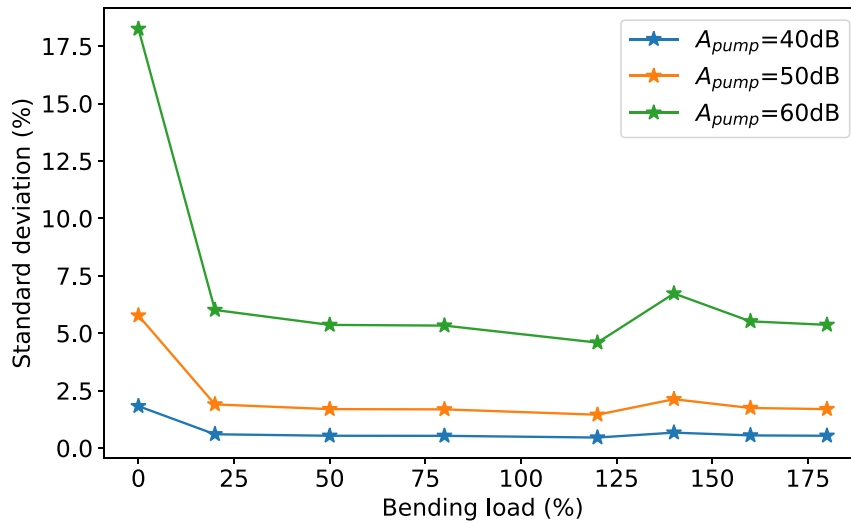


Fig. 7. Standard deviation of surface displacement velocity V_{disp} due to different pump waves amplitudes (40 dB, 50 dB, and 60 dB) at different static loading amplitudes.

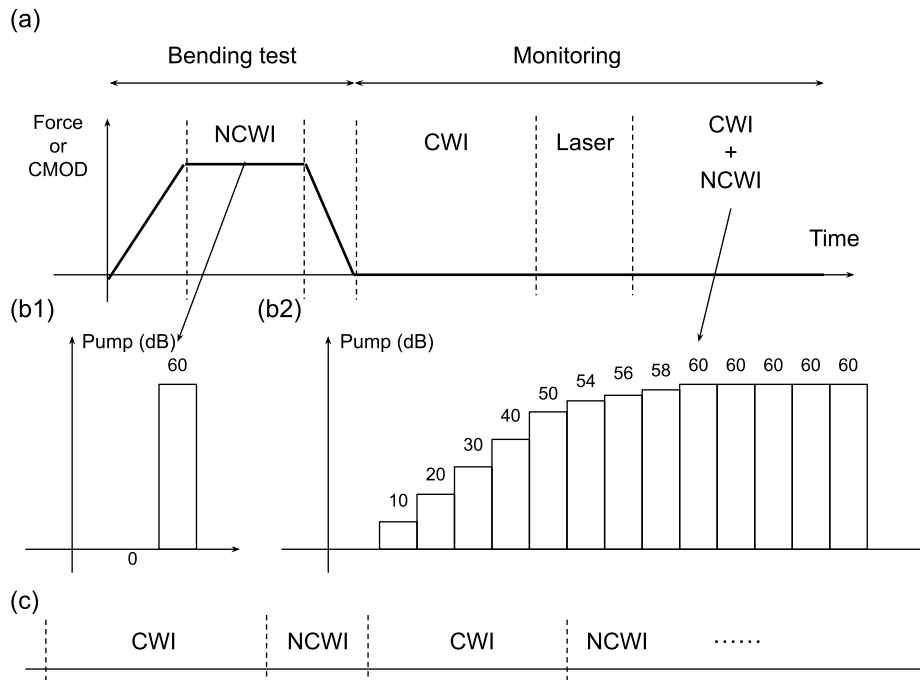


Fig. 8. (a) Schematic diagram of a single measurement cycle (bending test phase + monitoring phase). (b) evolution of the pump wave amplitude of NCWI during the creeping static load (b1) and during the monitoring phase (b2). (c) timeline of CWI and NCWI after laser measurement.

(S_p, R_q) couples, whereby the number of intersections is denoted N_{ij} . The nonlinearity level of each element (i,j) is then evaluated by the average of the product of NCWI observables and d_{ijpq} over the number of intersection N_{ij} .

$$\{\overline{\alpha_\theta}, \overline{\alpha_{K_d}}\}(x_i, y_j) = \begin{cases} 0 & \text{if } N_{ij} = 0 \\ \frac{1}{N_{ij}} \sum_{l=1}^{N_x} \sum_{j=1}^{N_y} \left[\sum_{p=1}^{N_{src}} \sum_{q=1}^{N_{recp}} \{\alpha_{\theta pq}, \alpha_{K_d pq}\} d_{ijpq} \right] & \text{if } N_{ij} \neq 0. \end{cases} \quad (5)$$

The macrocrack location can be indicated by the spatial distribution of $\overline{\alpha_\theta}$ and $\overline{\alpha_{K_d}}$ as defined by Eq. (5). To eliminate the error stemming from the initial state (0% bending load), all $\overline{\alpha_\theta}$ and $\overline{\alpha_{K_d}}$ values at 0% bending load are subtracted from the nonzero bending load results and normalized by their maximum spatial value, as shown in Eq. (6). This

operation, which might be challenging to perform on real structures, is optional and mainly aims at improving the interpretability of imaging results by enhancing the contrast.

$$\{\overline{\alpha_\theta}, \overline{\alpha_{K_d}}\}_{0\%}^{load\%} = \frac{\Delta\{\overline{\alpha_\theta}, \overline{\alpha_{K_d}}\}}{\max(\Delta\{\overline{\alpha_\theta}, \overline{\alpha_{K_d}}\})}, \quad (6)$$

where $\Delta\{\overline{\alpha_\theta}, \overline{\alpha_{K_d}}\} = \{\overline{\alpha_\theta}, \overline{\alpha_{K_d}}\}_{load\%} - \{\overline{\alpha_\theta}, \overline{\alpha_{K_d}}\}_{0\%}$.

2.4. Comparison to other techniques

2.4.1. Optical microscopy

In order to obtain the crack width and an approximate crack length after each loading cycle during the post-peak phase, an $\times 40$ optical microscopy image of the crack was taken on top of the notch after unloading. The crack length was then determined by measuring the distance from the notch to the position where no apparent aperture

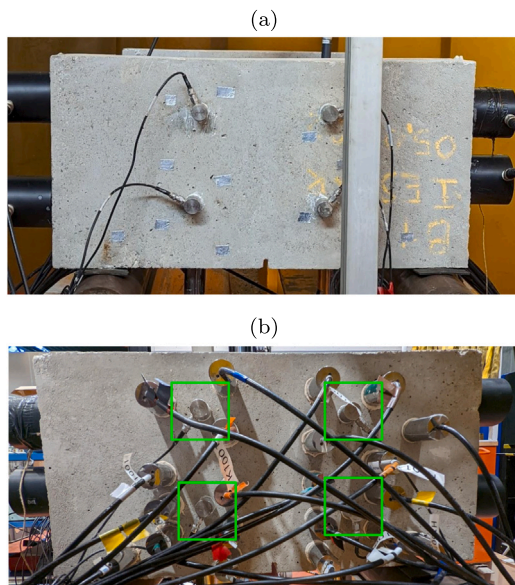


Fig. 9. AE transducers at front face (a) and rear face (b) face of inspected beam.

of the crack was present by moving the Hirox RH-2000 microscope along the crack. The crack length measurement by optical microscopy allowed drawing a comparison with both NCWI and AE results.

2.4.2. Acoustic Emission (AE) measurements

Piezoelectric transducers (R15 type) with a resonance frequency of 150 kHz were used to monitor the concrete beam cracking during the loading phases. These transducers were positioned around the expected location of crack propagation and glued using silicon grease to improve coupling with the concrete surface. The two main beam faces were instrumented with four transducers (Fig. 9).

AE signals were amplified with a 40 dB gain amplifier. The signals were converted by a PCI-card 8 and filtered with a low pass filter of 400 kHz and a high pass filter of 100 kHz. A sampling frequency of 1 MHz was adopted to acquire 2048 samples per AE signal. The threshold for signal detection lies at about 40 dB. The compression wave velocity was measured by evaluating time-of-flight pulses between transducers placed on each side of the concrete beam. Acoustic events were formed from a set of at least four signals.

Knowing the position of the transducers, the delay between signals, and the compression wave velocity, the localization of events could be determined by solving an error minimization problem between the recorded data and an estimated event with an assumed position [51].

3. Results and discussion

3.1. Optical microscopy results

The optical microscopy of the crack is recorded after each bending load application during the post-peak regime. The images are taken at different magnifications, and the crack size is characterized by: CMOD at the notch, maximum crack width within the selected zone and crack length. The values of these three parameters at each bending load level are listed in Table 2. From 120% to 180% bending load, the crack length increases from 0 cm to 14.9 cm. The 10-cm crack at 140% bending load is already close to half the beam's height, and the final crack length is greater than half the beam's height. In contrast, the crack aperture before 180% bending load is very small ($< 100 \mu\text{m}$), yet jumps to $200 \mu\text{m}$ at 180%. These results can also be directly observed in Fig. 10.

Table 2

Values of the optical microscopy parameters at each bending load level.

| Load | 120% | 140% | 160% | 180% |
|--|-------|-------|-------|--------|
| CMOD at notch (μm) | 20.51 | 39.23 | 60.82 | 121.76 |
| Maximum crack width within the selected zone (μm) | 25 | 65 | 84 | 200 |
| Crack length (cm) | \ | 10.0 | 12.7 | 14.9 |

3.2. AE results

3.2.1. AE energy analysis

The relationship between load or AE energy (normalized to the maximum value) and time for all load levels (50% to 180%) is displayed in Fig. 11, which indicates that the cumulative AE energy correlates well with loading level. The rate of AE energy is low at the beginning and increases until the load reaches a fixed level. This behavior is linear for the initial levels (50%, 80%, and 120%). In the pre-peak phase, no high energy release was observed due to the elastic behavior of the material. However, for load levels above 120%, the behavior starts with a flat pre-peak phase (very few detected hits), thus indicating a crack initiated before this level. This situation can be seen in Fig. 2, where the CMOD recorded at the notch did not return to its initial value after unloading, and moreover the difference between initial and final CMOD values increases with the bending load. The few detected hits at low energy are due to friction during opening of the existing crack. After this pre-peak phase, AE energy increases linearly due to crack propagation. In addition, a pre-peak phase duration increase related to crack opening is observed with respect to the load level. This duration increase is explained by the damage intensity, which increases with load level, thereby lengthening of the crack.

3.2.2. AE events analysis

The AE events density distribution provides an indication of the areas of acoustic activity due to concrete cracking. The density of AE events is calculated as the number of localized events on a $2 \text{ cm} \times 2 \text{ cm}$ surface. A threshold based on the amplitude of hits has been used to glean information about the intensity of the detected AE events.

The density of AE events has been plotted against the 2D localization maps of AE sources at load levels 120%, 140%, 160%, and 180%, respectively (Fig. 12 a to d). No AE events have been recorded at levels below the peak load. The analysis will thus focus on the four levels after the maximum load (i.e. 120% to 180%).

Beyond the maximum load, at the 120% load level, Fig. 12(a) shows very few detected AE events due to the damage that had begun to develop during the post-peak phase. In this phase, the events and energy density represent less than 3% of the total events and energy. In fact, cracks began to coalesce in the mortar matrix, exhibiting different realistic features, such as crack bridging in front of the notch due to stress concentration.

From the 140% load level in the post-peak region, the density of AE events considerably increases, indicating the presence of a crack located in the center of the specimen around $(25 \pm 2) \text{ cm}$. (see Fig. 12b), which corresponds to a detection of propagated cracks. This observation confirms the conclusion from the microscopic analysis presented in Section 3.1: a crack cannot be observed beyond a 120% load level, while, after the 140% load level, a crack approx. 10 cm high is observed at the beam center under the microscope, hence in agreement with the AE events localization.

In the post-peak region (up to 140% load), the number of AE events continues to increase, yet at a lower rate, thus indicating a stable crack propagation. It can also be observed that the AE density is higher at the core of the crack outlining the crack path. In addition, the AE events with greater amplitude ($> 70 \text{ dB}$) are more heavily concentrated in the crack path, thus corroborating crack presence near the vertical axis at $x = 25 \text{ cm}$. The localization of AE events with the highest

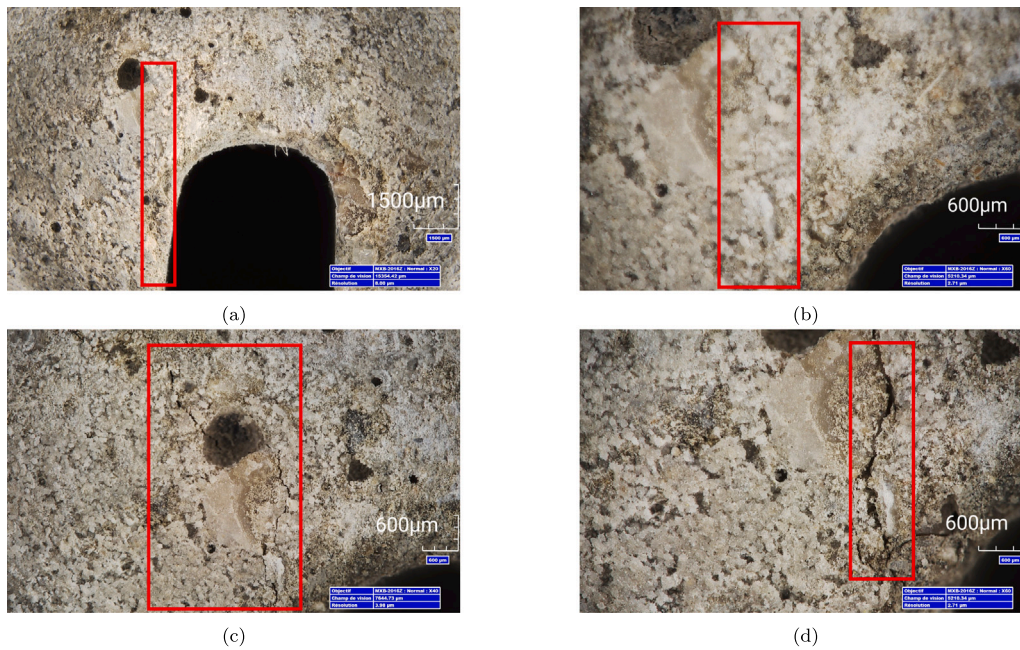


Fig. 10. Microscopic photography of the crack at four bending loads during the post-peak phase. (a) $120\%F_{max}$, (b) $140\%F_{max}$, (c) $160\%F_{max}$, (d) $180\%F_{max}$.

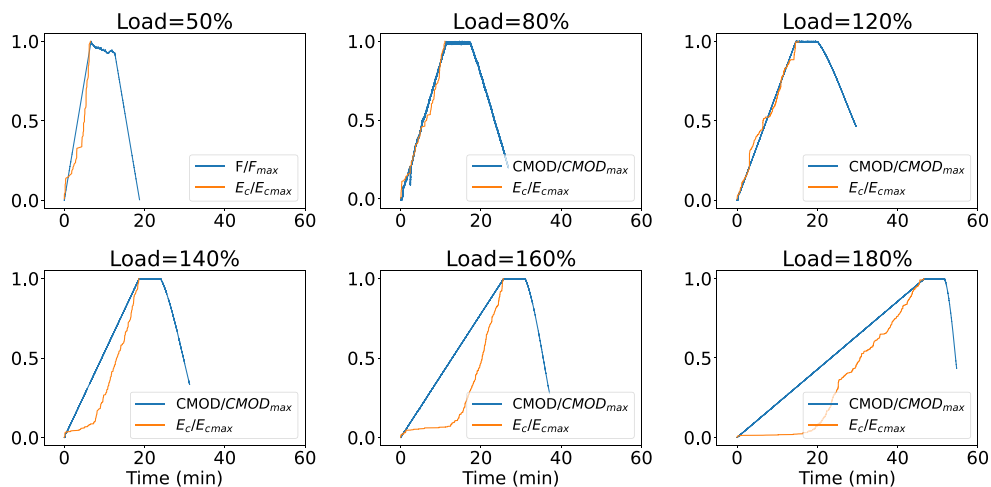


Fig. 11. Temporal evolution of normalized load and AE energy for various load levels.

amplitude is in good agreement with the crack length measured under the microscope. Indeed, the approximate crack length according to AE events localization can be estimated at around 13 cm to 14 cm and 15 cm to 17 cm for the 160% and 180% load levels, respectively, which closely matches the measured crack lengths using the microscope: 12.7 cm and 14.9 cm.

3.3. INCWI results

An example of the experimentally received coda signals recorded at various times during the pump wave excitation is exhibited in Fig. 13(a). Let us note that in the received coda signals, the difference between them is rather small during the early time (Fig. 13(b1)), and grows at later times (Fig. 13(b2)). This outcome is due to the variation of the relative propagation velocity of the concrete beam as well as to the cumulative effect of scattering property changes stemming from microcracking or macrocracking.

In relying on the example of source–receiver couple S5-R6, the results of the corresponding θ and K_d with respect to pump amplification

at 7 different bending load levels are presented in Fig. 14. It has been observed that the absolute value of θ increases with bending load level, moreover, the difference between the first two bending loads is very small and starts to increase significantly thereafter, which indicates that the nonzero values of θ before 50% bending load (weak though detectable by CWI) are very likely correlated with the nonlinearity of the concrete itself. The microcracking process due to bending load is initiated as of the 50% load level. The negative values of θ for all bending loads show that the microcrack or macrocrack generation leads to a local decrease in Young's modulus of the beam. For the K_d result, during the pre-peak phase (from 0% to 80% bending loads), the value of K_d is rather small (below 1%) compared to that of the post-peak phase (from 120% to 180% bending loads) by an order of magnitude. This finding reveals the much stronger impact of macrocrack generation on the wave scattering property than that of microcracks, whose impedance contrast between cracked and sound zones is significantly higher while the geometry change of the cracked zone is much more pronounced.

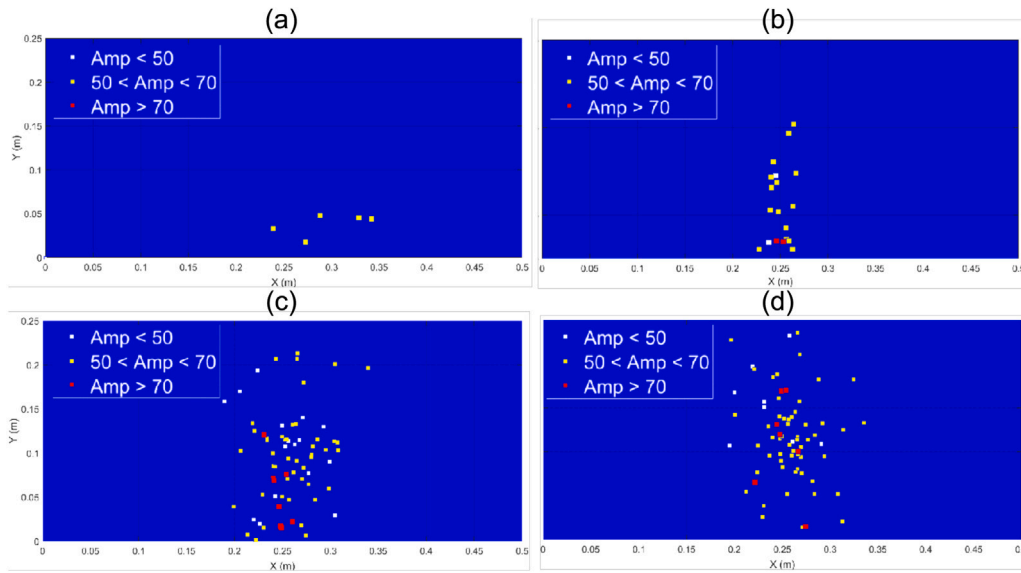


Fig. 12. Density of AE events at four different bending load levels: (a) $120\%F_{max}$, (b) $140\%F_{max}$, (c) $160\%F_{max}$, (d) $180\%F_{max}$.

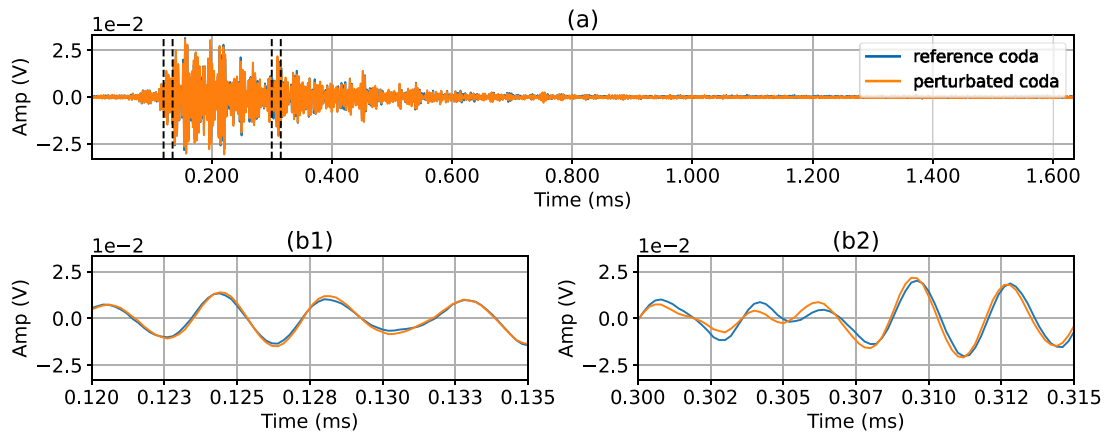


Fig. 13. Example of received coda signals at reference state (in blue, no pump wave) and perturbed state (in orange, nonzero amplitude pump wave), extracted from the NCWI test after the static bending load at 160% bending load. (a) Full reference and perturbed coda signals over an acquisition time of 1.6 ms. (b1) Zoom at early time between 0.12 ms and 0.135 ms. (b2) Zoom at late time between 0.3 ms and 0.315 ms. (For interpretation of the references to color in this figure legend, the reader is referred to the web version of this article.)

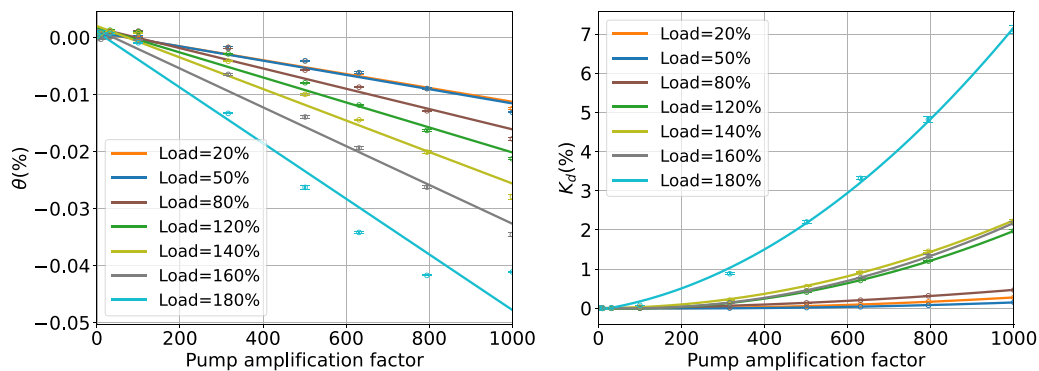


Fig. 14. θ and K_d with respect to pump wave amplification factor at 7 different bending load levels for source–receiver couple S5-R6.

Deeper experimental data analysis has been performed by extracting the α_{K_d} values for all source–receiver couples at 7 different bending load levels. The results of α_{K_d} with respect to all sources and receivers are presented in Fig. 15. Similar to the results in Fig. 14, the values of α_{K_d} are also smaller by an order of magnitude during the pre-peak

phase vs. the post-peak phase. During the post-peak phase, several source–receiver couples have consistently greater α_{K_d} values than their neighbors, e.g. S1-R14, S3-R14, S5-R14, S7-R14, as a result of the direct wave trajectories relative to these source–receiver couples intersecting with the crack located above the notch. On the other hand, the α_{K_d}

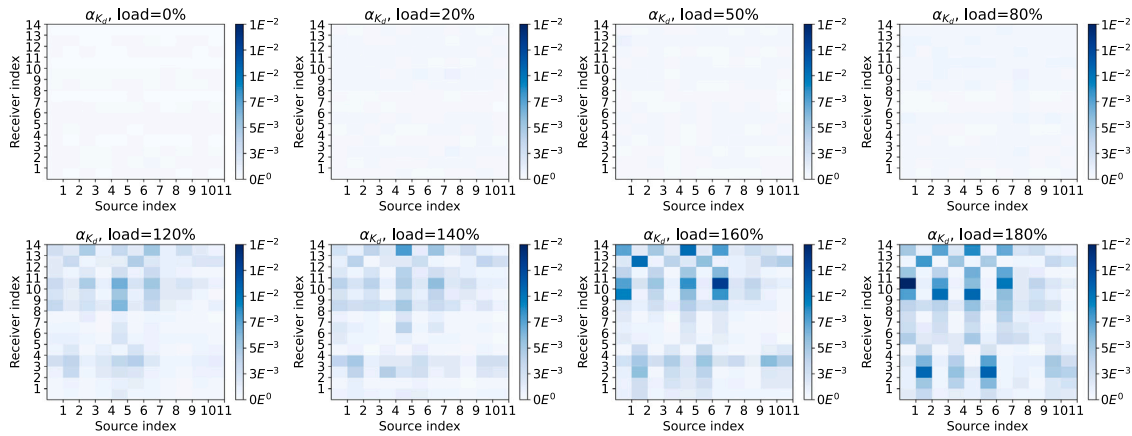


Fig. 15. Result of α_{K_d} with respect to source and receiver index at 8 different bending load levels.

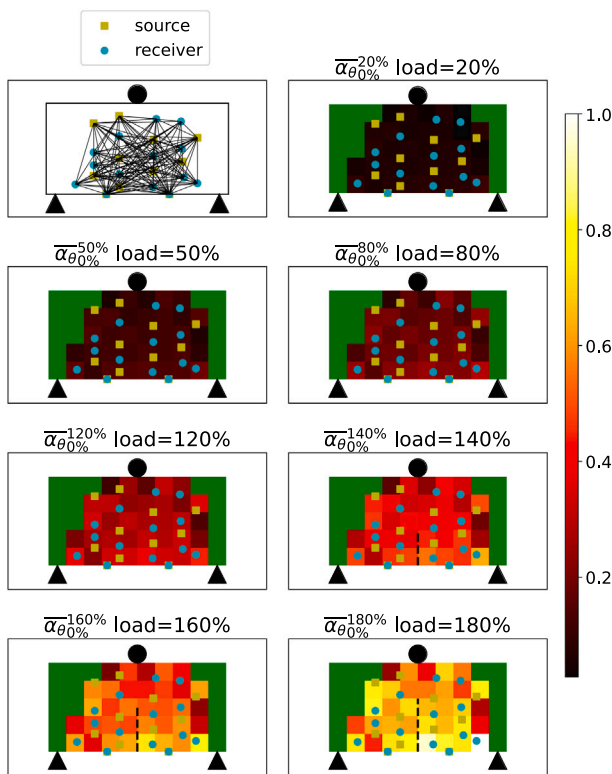


Fig. 16. Spatial distribution of $\overline{\alpha_{\theta}^{load\%}}$ at 7 different bending load levels ($\overline{\alpha_{\theta}^{load\%}}$). The black dashed line represents the experimentally measured macrocrack. Green elements represent the uncovered area (no transducers). (For interpretation of the references to color in this figure legend, the reader is referred to the web version of this article.)

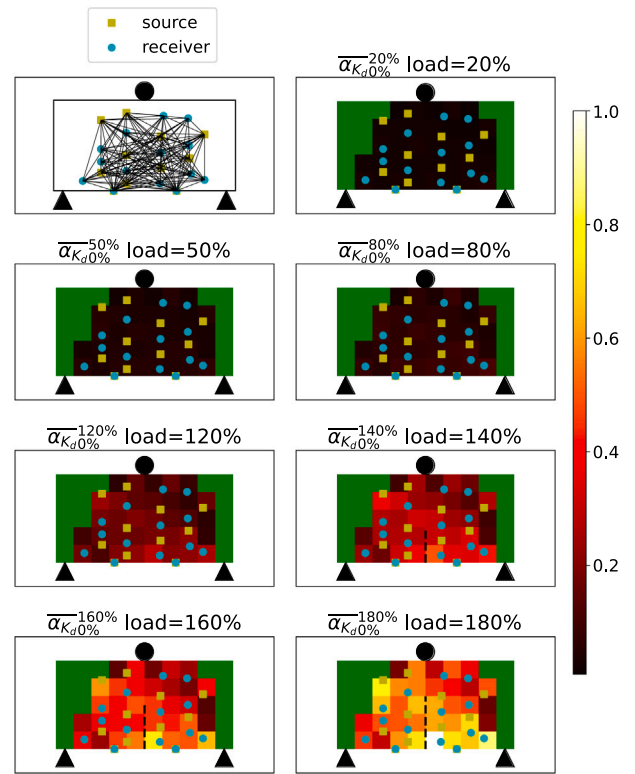


Fig. 17. Spatial distribution of $\overline{\alpha_{K_d}^{load\%}}$ at 7 different bending load levels ($\overline{\alpha_{K_d}^{load\%}}$). The black dashed line represents the experimentally measured macrocrack. Green elements represent the uncovered area (no transducers). (For interpretation of the references to color in this figure legend, the reader is referred to the web version of this article.)

values of some source–receiver couples become greater as the bending load increases, e.g. S1-R11, S3-R10, and S5-R10. This result is due to the macrocrack affecting those source–receiver couples closer to the force application point, where it can propagate further. Therefore, the α_{K_d} values are indeed consistent with experimental observations.

The 2D tomographies of $\overline{\alpha_{\theta}}$ and $\overline{\alpha_{K_d}}$, as defined in Eq. (6), are provided in Figs. 16 and 17 where $\max(\Delta\overline{\alpha_{\theta}}) \approx 0.031$ and $\max(\Delta\overline{\alpha_{K_d}}) \approx 0.094$, over which a normalization step is performed. During the post-peak phase, the notch at the bottom center can be observed by the gradient of $\overline{\alpha_{K_d}}$; also, the magnitudes of $\overline{\alpha_{\theta}}$ and $\overline{\alpha_{K_d}}$ increase with the bending load. Apart from the notch, the macrocrack at the lower center

is also in agreement with the experimentally observed macrocrack (dashed black line). During the pre-peak and post-peak phases (i.e. between 80% and 120% bending loads) as the nonlinear parameter increases by around 0.2 (from around 0.05 to 0.25) at some positions, while it increases by around 0.1 for $\overline{\alpha_{\theta}}$. Fig. 18 better illustrates the $\overline{\alpha_{\theta}}$ and $\overline{\alpha_{K_d}}$ values with respect to the bending load level at various locations. At all horizontal and vertical locations, an abrupt

More interestingly, it can be noticed that $\overline{\alpha_{K_d}}$ is more sensitive to the macrocrack generation than $\overline{\alpha_{\theta}}$ between the pre-peak and post-peak phases (i.e. between 80% and 120% bending loads) as the nonlinear parameter increases by around 0.2 (from around 0.05 to 0.25) at some positions, while it increases by around 0.1 for $\overline{\alpha_{\theta}}$. Fig. 18 better illustrates the $\overline{\alpha_{\theta}}$ and $\overline{\alpha_{K_d}}$ values with respect to the bending load level at various locations. At all horizontal and vertical locations, an abrupt

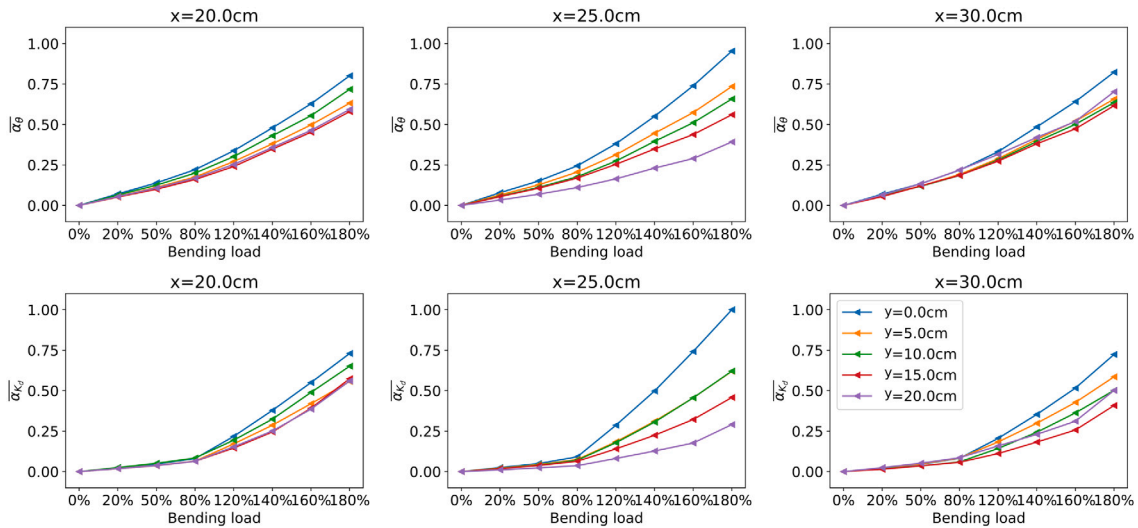


Fig. 18. Evolution of $\bar{\alpha}_\theta$ and $\bar{\alpha}_{K_d}$ with respect to bending at 3 horizontal (x) and 5 vertical (y) locations.

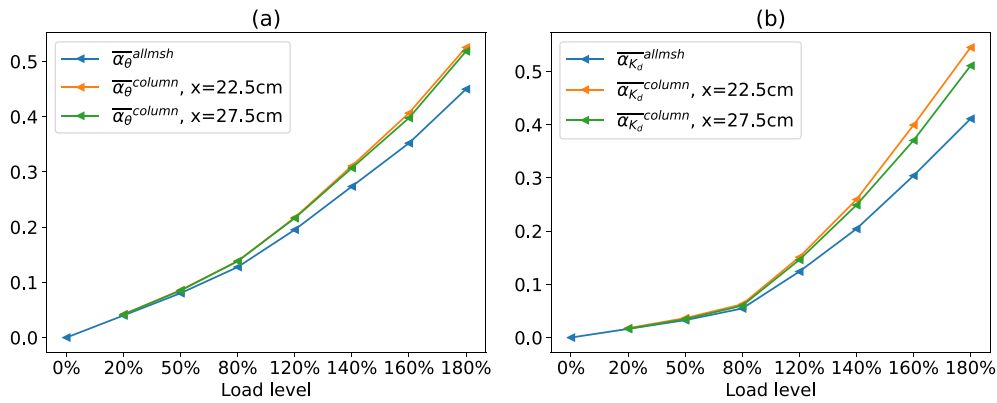


Fig. 19. Evolution of INCWI parameters with respect to load level. (a) $\bar{\alpha}_\theta^{allmsh}$ and $\bar{\alpha}_\theta^{column}$, (b) $\bar{\alpha}_{K_d}^{allmsh}$ and $\bar{\alpha}_{K_d}^{column}$ at $x = 22.5$ cm and $x = 27.5$ cm.

variation is observed in $\bar{\alpha}_{K_d}$ while $\bar{\alpha}_\theta$ increases smoothly. The rationale for this result is that macrocrack generation pertains to a change in geometry; furthermore, $\bar{\alpha}_{K_d}$ is sensitive to scattering property changes while $\bar{\alpha}_\theta$ is more closely correlated with the effective Young's modulus variation. At a central location $x = 25$ cm, the amplitudes of $\bar{\alpha}_\theta$ and $\bar{\alpha}_{K_d}$ decrease when the vertical location y rises. This observation is in good agreement with the actual case, whereby the nonlinearity level decreases as the recording point moves further from the notch.

3.4. Comparative analysis of AE and INCWI results

In order to verify the robustness of the new INCWI method, a comparison between AE and INCWI results has been carried out and will be discussed in this section. Each method has been evaluated according to one or more chosen parameters. For AE, the chosen parameter was the number of AE events capable of being retrieved from Fig. 12; it reflects the overall damage level caused by geometry changes due to crack generation. As for INCWI, the chosen parameters needed to be equally representative as the number of AE events in terms of evaluating the level of nonlinearity. Several INCWI parameters were investigated, the first ones being the averages of $\bar{\alpha}_\theta$ and $\bar{\alpha}_{K_d}$ over all elements of the mesh ($\bar{\alpha}_\theta^{allmsh}$ and $\bar{\alpha}_{K_d}^{allmsh}$), the second ones being the averages of $\bar{\alpha}_\theta$ and $\bar{\alpha}_{K_d}$ over just those elements in each mesh column ($\bar{\alpha}_\theta^{column}$ and $\bar{\alpha}_{K_d}^{column}$). $\bar{\alpha}_\theta^{allmsh}$ and $\bar{\alpha}_{K_d}^{allmsh}$ provide a global view of this level,

while $\bar{\alpha}_\theta^{column}$ and $\bar{\alpha}_{K_d}^{column}$ show the horizontal location dependency of the nonlinearity level. Both types of parameters can be compared with the number of AE events, while $\bar{\alpha}_\theta^{column}$ and $\bar{\alpha}_{K_d}^{column}$ need to be chosen at a specific horizontal location x . The results of $\bar{\alpha}_{\theta, K_d}^{allmsh}$ and $\bar{\alpha}_{\theta, K_d}^{column}$ are illustrated in Figs. 19 and 20. Fig. 19 reveals that regardless of the average over all mesh elements, $\bar{\alpha}_\theta^{allmsh}$ retains similar signatures as in Fig. 18, which means that the abrupt gradient change of $\bar{\alpha}_{K_d}$ between pre-peak and post-peak phases (i.e. between 80% load and 120% load) does not depend on observation location; rather, it is determined by its sensitivity to geometry change. As for Fig. 20, similarly to Figs. 16 and 17, the most heavily damaged zone lies at the central location $x = 22.5$ cm and $x = 27.5$ cm, the nonlinearity level decreases when moving away from the center. This observation agrees with the contents of Fig. 12. The sections of Fig. 20 at $x = 22.5$ cm and $x = 27.5$ cm are illustrated in Fig. 19, they have the same signatures as in Figs. 18 and 19. Since it is preferable to choose only a single x axis position to compare with AE results, the most heavily damaged location $x = 22.5$ cm is chosen for $\bar{\alpha}_{\theta, K_d}^{column}$, as denoted $\bar{\alpha}_{\theta, K_d}^{column, center}$.

The evolution of the number of AE events and INCWI parameters with respect to the load level during the post-peak phase is given in Fig. 21. All INCWI parameters follow a rather similar evolution signature as that of the number of AE events. In order to evaluate the level of correlation between the number of AE events and INCWI

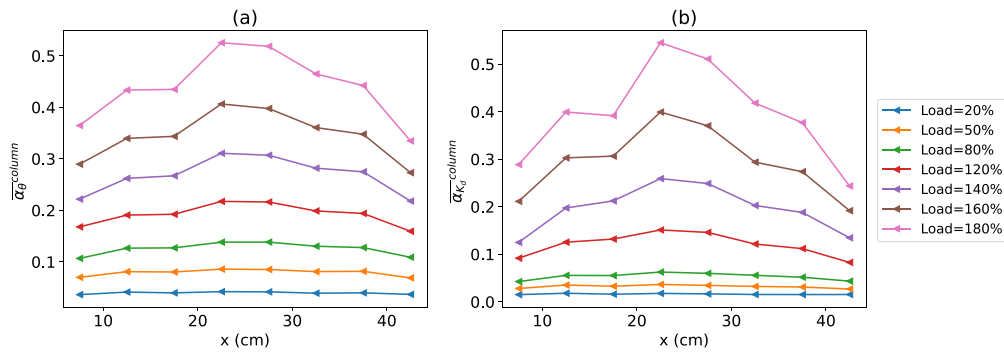


Fig. 20. (a) $\overline{\alpha_{\theta}^{column}}$ and (b) $\overline{\alpha_{K_d}^{column}}$ with respect to horizontal element location under different load levels.

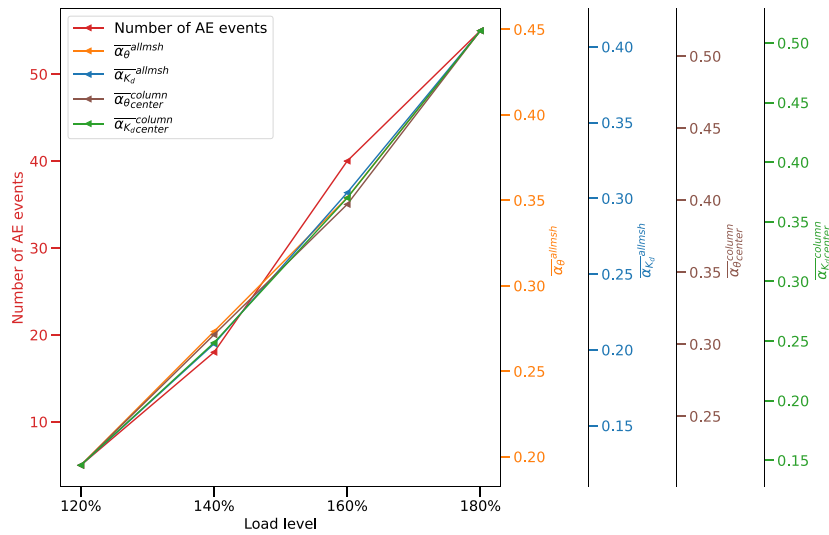


Fig. 21. Number of AE events and INCWI parameters with respect to load level during post-peak phase.

parameters, one approach would be to use the Pearson correlation coefficient r , which is above 0.97 for all INCWI parameters ($r_{\overline{\alpha_{\theta}^{allmsh}}}$, $r_{\overline{\alpha_{\theta}^{column}}}$, $r_{\overline{\alpha_{\theta}^{center}}}$, $r_{\overline{\alpha_{K_d}^{allmsh}}}$, $r_{\overline{\alpha_{K_d}^{column}}}$, and $r_{\overline{\alpha_{K_d}^{center}}}$). All INCWI parameters are highly correlated with the number of AE events (values nearly greater than 0.5). In particular, the correlation between $\overline{\alpha_{K_d}^{column}}$ and the number of AE events is slightly stronger than with $\overline{\alpha_{\theta}^{center}}$, which is most likely because both $\overline{\alpha_{K_d}^{column}}$ and AE events require geometry changes while $\overline{\alpha_{\theta}^{center}}$ is also sensitive to non geometry changes, e.g. local Young’s modulus variation.

4. Conclusion

This study has introduced an imaging algorithm, called INCWI for “Imaging using NCWI” in order to localize cracks in concrete using NCWI outputs along with a spatial averaging method. The spatial average takes into account all NCWI parameters α_{θ} and α_{K_d} of each source–receiver couple and outputs the averaged parameters $\overline{\alpha_{\theta}}$ and $\overline{\alpha_{K_d}}$. In this aim, a crack was generated in a concrete beam by means of three-point bending. The beam was then loaded several times at 20%, 50% and 80% of the reference ultimate load in the pre-peak regime and 120%, 140%, 160% and 180% in the post-peak regime using CMOD control. INCWI tests were conducted to obtain several NCWI outputs for various source–receiver couples. A comparison was drawn with the acoustic emission (AE) technique run during each loading phase and with the microscopic imaging performed after unloading, which provided information on crack geometry, e.g., width and height.

The main results of this study can be summarized as follows:

- INCWI allows for the localization of cracks, from very thin to relatively large and long cracks. Thus, crack propagation monitoring in concrete can be achieved for closed and partially open cracks without any external load.
- A better sensitivity of $\overline{\alpha_{K_d}}$ to the crack formation was found thanks to the quadratic relationship with crack width as well as its sensibility to scattering property changes, which are strongly correlated with changes in geometry.
- NCWI results can capture weak changes during the pre-peak phase when damage stems mainly from microcracks, which has hardly been observed in AE results.
- The evolution of $\overline{\alpha_{K_d}}$ contains a gradient change between the pre-peak phase and post-peak phase, as compared to $\overline{\alpha_{\theta}}$, which originates from the sensitivity of $\overline{\alpha_{K_d}}$ to geometry changes from macrocrack generation.
- INCWI agrees with AE and optical microscopy techniques during the post-peak phase since the technique can grasp gradual propagation, i.e. height increase and enlargement, of the cracks during the post-peak regime. Similarly to AE, which can locate a crack in a volume during its creation without any prior knowledge of its location, INCWI is able to locate an existing crack even with a limited width. Furthermore, when the crack opens and extends in height due to loading, INCWI outputs agree with both AE and optical microscopy observations.

In future works, several perspectives may be considered in an effort to improve our current imaging method. For instance, a coupling of the

INCWI method with the analytical solutions of NCWI parameters with respect to bending load could be useful to demonstrate the robustness of the INCWI method at both the theoretical and numerical levels. INCWI can also be extended to the 3D imaging of cracks by taking advantage of imaging algorithms developed for linear coda wave interferometry, with application to micro or macrocrack detection on in-situ structures.

CRedit authorship contribution statement

Shilin Qu: Conceptualization, Investigation, Formal analysis, Visualization, Software, Writing – original draft. **Benoît Hilloulin:** Conceptualization, Investigation, Methodology, Writing – original draft, Writing – review & editing, Validation, Resources, Supervision. **Jacqueline Saliba:** Conceptualization, Investigation. **Mehdi Sbartai:** Conceptualization, Formal analysis, Visualization, Validation, Writing – original draft. **Odile Abraham:** Conceptualization, Validation, Supervision, Writing – review & editing, Project administration, Funding acquisition. **Vincent Tournat:** Supervision, Writing – review & editing.

Declaration of competing interest

The authors declare that they have no known competing financial interests or personal relationships that could have appeared to influence the work reported in this paper.

Data availability

The data that has been used is confidential.

Acknowledgments

The authors would like to thank Olivier DURAND (GeoEND, Université Gustave Eiffel) as well as Vincent WISNIEWSKI and Mathias MARCEL (GeM, Ecole Centrale de Nantes) for their valuable assistance during the experimental campaign.

References

- [1] Karl Wiegink, Shashidhara Marikunte, Surendra P. Shah, Shrinkage cracking of high-strength concrete, *Mater. J.* 93 (5) (1996) 409–415.
- [2] Yilmaz Akkaya, Chengsheng Ouyang, Surendra P. Shah, Effect of supplementary cementitious materials on shrinkage and crack development in concrete, *Cem. Concr. Compos.* (ISSN: 0958-9465) 29 (2) (2007) 117–123, <http://dx.doi.org/10.1016/j.cemconcomp.2006.10.003>, URL: <https://www.sciencedirect.com/science/article/pii/S0958946506001818>.
- [3] Judy Kheir, Anja Estensen Klausen, Tor Arne Hammer, Laurence De Meyst, Benoit Hilloulin, Kim Van Tittelboom, Ahmed Loukili, Nele De Belie, Early age autogenous shrinkage cracking risk of an ultra-high performance concrete (UHPC) wall: Modelling and experimental results, *Eng. Fract. Mech.* (ISSN: 0013-7944) 257 (2021) 108024, <http://dx.doi.org/10.1016/j.engfracmech.2021.108024>, URL: <https://www.sciencedirect.com/science/article/pii/S0013794421004458>.
- [4] Graciela Giaccio, Raúl Luis Zerbino, Juan Manuel Ponce, Oscar Batic, Mechanical behavior of concretes damaged by alkali-silica reaction, *Cem. Concr. Res.* (ISSN: 0008-8846) 38 (7) (2008) 993–1004, <http://dx.doi.org/10.1016/j.cemconres.2008.02.009>, URL: <https://www.sciencedirect.com/science/article/pii/S0008884608000537>.
- [5] Xavier Brunetaud, R Linder, L Divet, D Duragrin, D Damidot, Effect of curing conditions and concrete mix design on the expansion generated by delayed ettringite formation, *Mater. Struct.* 40 (6) (2007) 567–578.
- [6] Ismail Aldellaa, Petr Havlásek, Milan Jirásek, Peter Grassl, Effect of creep on corrosion-induced cracking, *Eng. Fract. Mech.* (ISSN: 0013-7944) 264 (2022) 108310, <http://dx.doi.org/10.1016/j.engfracmech.2022.108310>, URL: <https://www.sciencedirect.com/science/article/pii/S0013794422000704>.
- [7] Yuqi Zhou, Weiyei Chen, Peiyu Yan, Measurement and modeling of creep property of high-strength concrete considering stress relaxation effect, *J. Build. Eng.* (ISSN: 2352-7102) 56 (2022) 104726, <http://dx.doi.org/10.1016/j.job.2022.104726>, URL: <https://www.sciencedirect.com/science/article/pii/S23527102220007392>.
- [8] Shuang Peng, Zoubir Mehdi Sbartai, Thomas Parent, Mechanical damage evaluation of masonry under tensile loading by acoustic emission technique, *Constr. Build. Mater.* (ISSN: 0950-0618) 258 (2020) 120336, <http://dx.doi.org/10.1016/j.conbuildmat.2020.120336>, URL: <https://www.sciencedirect.com/science/article/pii/S0950061820323412>.
- [9] Shiyuan Ju, Dongsheng Li, Jinqing Jia, Machine-learning-based methods for crack classification using acoustic emission technique, *Mech. Syst. Signal Process.* (ISSN: 0888-3270) 178 (2022) 109253, <http://dx.doi.org/10.1016/j.jymssp.2022.109253>, URL: <https://www.sciencedirect.com/science/article/pii/S0888327022004010>.
- [10] Lin Kong, ZhaoFeng Lu, ZhaoYi He, ZuZhen Shen, Hao Xu, Kang Yang, Le Yu, Characterization of crack resistance mechanism of fiber modified emulsified asphalt cold recycling mixture based on acoustic emission parameters, *Constr. Build. Mater.* (ISSN: 0950-0618) 327 (2022) 126939, <http://dx.doi.org/10.1016/j.conbuildmat.2022.126939>, URL: <https://www.sciencedirect.com/science/article/pii/S0950061822006249>.
- [11] Zhanming Shi, Jiangteng Li, Ju Wang, Effect of creep load on fatigue behavior and acoustic emission characteristics of sandstone containing pre-existing crack during fatigue loading, *Theor. Appl. Fract. Mech.* (ISSN: 0167-8442) 119 (2022) 103296, <http://dx.doi.org/10.1016/j.tafmec.2022.103296>, URL: <https://www.sciencedirect.com/science/article/pii/S0167844222000490>.
- [12] Xiaoran Wang, Enyuan Wang, Xiaofei Liu, Damage characterization of concrete under multi-step loading by integrated ultrasonic and acoustic emission techniques, *Constr. Build. Mater.* (ISSN: 0950-0618) 221 (2019) 678–690, <http://dx.doi.org/10.1016/j.conbuildmat.2019.06.105>, URL: <https://www.sciencedirect.com/science/article/pii/S0950061819315351>.
- [13] Bassim El Jazouli, Eleni Tsangouri, Fire-exposed stones in constructions: Residual strength, performance loss and damage mode shift due to mineralogical transformation and micro-cracking, *Eng. Geol.* (ISSN: 0013-7952) 302 (2022) 106638, <http://dx.doi.org/10.1016/j.enggeo.2022.106638>, URL: <https://www.sciencedirect.com/science/article/pii/S0013795222001235>.
- [14] Harshbab Singh, Rishi Gupta, Cellulose fiber as bacteria-carrier in mortar: Self-healing quantification using UPV, *J. Build. Eng.* (ISSN: 2352-7102) 28 (2020) 101090, <http://dx.doi.org/10.1016/j.job.2019.101090>, URL: <https://www.sciencedirect.com/science/article/pii/S2352710219313336>.
- [15] Tai-Ming He, Qi Zhao, Johnson Ha, Kaiwen Xia, Giovanni Grasselli, Understanding progressive rock failure and associated seismicity using ultrasonic tomography and numerical simulation, *Tunn. Undergr. Space Technol.* (ISSN: 0886-7798) 81 (2018) 26–34, <http://dx.doi.org/10.1016/j.tust.2018.06.022>, URL: <https://www.sciencedirect.com/science/article/pii/S0886779817303309>.
- [16] Yifan Zhang, Farhad Aslani, Barry Lehane, Compressive strength of rubberized concrete: Regression and GA-BPNN approaches using ultrasonic pulse velocity, *Constr. Build. Mater.* (ISSN: 0950-0618) 307 (2021) 124951, <http://dx.doi.org/10.1016/j.conbuildmat.2021.124951>, URL: <https://www.sciencedirect.com/science/article/pii/S095006182102701X>.
- [17] Lotfollah Pahlavan, Fengqiao Zhang, Gerrit Blacquièrre, Yuguang Yang, DA Dick Hordijk, Interaction of ultrasonic waves with partially-closed cracks in concrete structures, *Constr. Build. Mater.* 167 (2018) 899–906.
- [18] Eunjong Ahn, Hyunjun Kim, Sung-Han Sim, Sung woo Shin, John S. Popovics, Myoungsu Shin, Surface-wave based model for estimation of discontinuity depth in concrete, *Sensors (Basel, Switzerland)* 18 (2018).
- [19] Foo Wei Lee, Hwa Kian Chai, Kok Sing Lim, Characterizing concrete surface notch using Rayleigh wave phase velocity and wavelet parametric analyses, *Constr. Build. Mater.* (ISSN: 0950-0618) 136 (2017) 627–642, <http://dx.doi.org/10.1016/j.conbuildmat.2016.08.145>, URL: <https://www.sciencedirect.com/science/article/pii/S0950061816314088>.
- [20] Dariusz Broda, Wiesław Jerzy Staszewski, Adam Martowicz, Tadeusz Uhl, Vadim Silberschmidt, Modelling of nonlinear crack-wave interactions for damage detection based on ultrasound—A review, *J. Sound Vib.* (ISSN: 0022-460X) 333 (4) (2014) 1097–1118, <http://dx.doi.org/10.1016/j.jsv.2013.09.033>, URL: <https://www.sciencedirect.com/science/article/pii/S0022460X13007876>.
- [21] Keith Worden, Nonlinearity in Structural Dynamics: Detection, Identification and Modelling, CRC Press, Boca Raton, ISBN: 978-0-429-13833-1, 2001, <http://dx.doi.org/10.1201/9780429138331>.
- [22] Maosen Cao, Qitian Lu, Zhongqing Su, Maciej Radziński, Wei Xu, Wiesław Ostachowicz, A nonlinearity-sensitive approach for detection of “breathing” cracks relying on energy modulation effect, *J. Sound Vib.* (ISSN: 0022-460X) 524 (2022) 116754, <http://dx.doi.org/10.1016/j.jsv.2022.116754>, URL: <https://www.sciencedirect.com/science/article/pii/S0022460X22000104>.
- [23] Wei Xu, Zhongqing Su, Maciej Radziński, Maosen Cao, Wiesław Ostachowicz, Nonlinear pseudo-force in a breathing crack to generate harmonics, *J. Sound Vib.* (ISSN: 0022-460X) 492 (2021) 115734, <http://dx.doi.org/10.1016/j.jsv.2020.115734>, URL: <https://www.sciencedirect.com/science/article/pii/S0022460X20305642>.
- [24] Philippe Blanloeuil, Anissa Meziane, Christophe Bacon, Numerical study of nonlinear interaction between a crack and elastic waves under an oblique incidence, *Wave Motion* (ISSN: 0165-2125) 51 (3) (2014) 425–437, <http://dx.doi.org/10.1016/j.wavemoti.2013.10.002>, URL: <https://www.sciencedirect.com/science/article/pii/S0165212513001613>.
- [25] Philippe Blanloeuil, Anthony J. Croxford, Anissa Meziane, Numerical and experimental study of the nonlinear interaction between a shear wave and a frictional interface, *J. Acoust. Soc. Am.* 135 (4) (2014) 1709–1716, <http://dx.doi.org/10.1121/1.4868402>.

- [26] Shilin Qu, Benoît Hilloulin, Olivier Chupin, Jean-Michel Piau, Odile Abraham, Vincent Tournat, Towards quantifying the effect of pump wave amplitude on cracks in the nonlinear coda wave interferometry method, *Ultrasonics* (ISSN: 0041-624X) 132, 106991, <http://dx.doi.org/10.1016/j.ultras.2023.106991>, URL: <https://linkinghub.elsevier.com/retrieve/pii/S0041624X23000677>.
- [27] Jiang Jin, Jacques Rivière, Yoshikazu Ohara, Parisa Shokouhi, Dynamic acousto-elastic response of single fatigue cracks with different microstructural features: An experimental investigation, *J. Appl. Phys.* 124 (7) (2018) 075303, <http://dx.doi.org/10.1063/1.5036531>.
- [28] Nikolay Smagin, Andrey Trifonov, Olivier Bou Matar, Vladislav Aleshin, Local damage detection by nonlinear coda wave interferometry combined with time reversal, *Ultrasonics* (ISSN: 0041-624X) 108 (2020) 106226, <http://dx.doi.org/10.1016/j.ultras.2020.106226>, URL: <https://www.sciencedirect.com/science/article/pii/S0041624X20301657>.
- [29] Martin Lott, Marcel C. Remillieux, Vincent Garnier, T.J. Ulrich, Pierre-Yves Le Bas, Arnaud Deraemaeker, Cédric Dumoulin, Cédric Payan, Fracture processes imaging in concrete using nonlinear ultrasound, *NDT & E Int.* (ISSN: 0963-8695) 120 (2021) 102432, <http://dx.doi.org/10.1016/j.ndteint.2021.102432>, URL: <https://www.sciencedirect.com/science/article/pii/S0963869521000311>.
- [30] Jichao Xu, Wujun Zhu, Yanxun Xiang, Yang Gao, Xunlin Qiu, Localization and imaging of micro-cracks using nonlinear lamb waves with imperfect group-velocity matching, *Appl. Sci.* (ISSN: 2076-3417) 11 (17) (2021) <http://dx.doi.org/10.3390/app11178069>, URL: <https://www.mdpi.com/2076-3417/11/17/8069>.
- [31] Qi Xue, Eric Larose, Ludovic Moreau, Locating structural changes in a multiple scattering domain with an irregular shape, *J. Acoust. Soc. Am.* (ISSN: 0001-4966) 146 (1) (2019) 595–602, <http://dx.doi.org/10.1121/1.5118246>.
- [32] Stefan Grabke, Kai-Uwe Bletzinger, Roland Wüchner, Development of a finite element-based damage localization technique for concrete by applying coda wave interferometry, *Eng. Struct.* (ISSN: 0141-0296) 269 (2022) 114585, <http://dx.doi.org/10.1016/j.engstruct.2022.114585>, URL: <https://www.sciencedirect.com/science/article/pii/S0141029622006885>.
- [33] Yuxiang Zhang, Vincent Tournat, Odile Abraham, Olivier Durand, Stéphane Letourneur, Alain Le Duff, Bertrand Lascoup, Nonlinear mixing of ultrasonic coda waves with lower frequency-swept pump waves for a global detection of defects in multiple scattering media, *J. Appl. Phys.* 113 (6) (2013) 064905, <http://dx.doi.org/10.1063/1.4791585>.
- [34] Guangzhi Chen, Damien Pageot, Jean-Baptiste Legland, Odile Abraham, Mathieu Chekroun, Vincent Tournat, Numerical modeling of ultrasonic coda wave interferometry in a multiple scattering medium with a localized nonlinear defect, *Wave Motion* 72 (2017) 228–243.
- [35] Yuxiang Zhang, Vincent Tournat, Odile Abraham, Olivier Durand, Stéphane Letourneur, Alain Le Duff, Bertrand Lascoup, Nonlinear coda wave interferometry for the global evaluation of damage levels in complex solids, *Ultrasonics* (ISSN: 0041-624X) 73 (2017) 245–252, <http://dx.doi.org/10.1016/j.ultras.2016.09.015>, URL: <https://www.sciencedirect.com/science/article/pii/S0041624X16301950>.
- [36] Shukui Liu, Bin Ma, Zhanguo Ma, Junbo Sun, Qi ang Wang, Keliang Liu, Evaluation of the compressional damage evolution of ancient fired clay bricks using coda wave analysis, *J. Build. Eng.* (ISSN: 2352-7102) 49 (2022) 104071, <http://dx.doi.org/10.1016/j.jobbe.2022.104071>, URL: <https://www.sciencedirect.com/science/article/pii/S2352710222000845>.
- [37] Benoît Hilloulin, Yuxiang Zhang, Odile Abraham, Ahmed Loukili, Frédéric Grondin, Olivier Durand, Vincent Tournat, Small crack detection in cementitious materials using nonlinear coda wave modulation, *NDT & E Int.* (ISSN: 0963-8695) 68 (2014) 98–104, <http://dx.doi.org/10.1016/j.ndteint.2014.08.010>, URL: <https://www.sciencedirect.com/science/article/pii/S0963869514001133>.
- [38] Maxime Farin, Emmanuel Moulin, Lynda Chehami, Farouk Benmeddour, Cyril Nicard, Pierre Campistrion, Olivier Bréhault, Lucie Dupont, Monitoring saltwater corrosion of steel using ultrasonic coda wave interferometry with temperature control, *Ultrasonics* (ISSN: 0041-624X) 124 (2022) 106753, <http://dx.doi.org/10.1016/j.ultras.2022.106753>, URL: <https://www.sciencedirect.com/science/article/pii/S0041624X22000634>.
- [39] Yuxiang Zhang, Thomas Planès, Eric Larose, Anne Obermann, Claude Rospars, Gautier Moreau, Diffuse ultrasound monitoring of stress and damage development on a 15-ton concrete beam, *J. Acoust. Soc. Am.* 139 (4) (2016) 1691–1701, <http://dx.doi.org/10.1121/1.4945097>.
- [40] Christoph Sens-Schönfelder, Éric Larose, Temporal changes in the lunar soil from correlation of diffuse vibrations, *Phys. Rev. E* 78 4 Pt 2 (2008) 045601.
- [41] Tejas H. Patel, Ashish K. Darpe, Influence of crack breathing model on nonlinear dynamics of a cracked rotor, *J. Sound Vib.* (ISSN: 0022-460X) 311 (3) (2008) 953–972, <http://dx.doi.org/10.1016/j.jsv.2007.09.033>, URL: <https://www.sciencedirect.com/science/article/pii/S0022460X0700781X>.
- [42] Thomas G. Chondros, Andrew D. Damarogonas, Jonathan Yao, Vibration of a beam with a breathing crack, *J. Sound Vib.* (ISSN: 0022-460X) 239 (1) (2001) 57–67, <http://dx.doi.org/10.1006/jsvi.2000.3156>, URL: <https://www.sciencedirect.com/science/article/pii/S0022460X00931560>.
- [43] Kai Wang, Menglong Liu, Zhongqing Su, Shenfang Yuan, Zheng Fan, Analytical insight into “breathing” crack-induced acoustic nonlinearity with an application to quantitative evaluation of contact cracks, *Ultrasonics* (ISSN: 0041-624X) 88 (2018) 157–167, <http://dx.doi.org/10.1016/j.ultras.2018.03.008>, URL: <https://www.sciencedirect.com/science/article/pii/S0041624X17310272>.
- [44] Christophe Sens-Schönfelder, Ulrich Wegler, Passive image interferometry and seasonal variations of seismic velocities at Merapi Volcano, Indonesia, *Geophys. Res. Lett.* 33 (21) (2006) <http://dx.doi.org/10.1029/2006GL027797>, <https://agupubs.onlinelibrary.wiley.com/doi/pdf/10.1029/2006GL027797>, URL: <https://agupubs.onlinelibrary.wiley.com/doi/abs/10.1029/2006GL027797>.
- [45] Yuxiang Zhang, Odile Abraham, Vincent Tournat, Alain Le Duff, Bertrand Lascoup, Ahmed Loukili, Frédéric Grondin, Olivier Durand, Validation of a thermal bias control technique for coda wave interferometry (CWI), *Ultrasonics* (ISSN: 0041-624X) 53 (3) 658–664, <http://dx.doi.org/10.1016/j.ultras.2012.08.003>, URL: <http://www.sciencedirect.com/science/article/pii/S0041624X12001564>, ZSCC: 0000071.
- [46] Yuxiang Zhang, Eric Larose, Ludovic Moreau, Grégoire d’Ozouville, Three-dimensional in-situ imaging of cracks in concrete using diffuse ultrasound, *Struct. Health Monit.* (ISSN: 1475-9217) 17 (2) 279–284, <http://dx.doi.org/10.1177/1475921717690938>, ZSCC:00036 Publisher: SAGE Publications.
- [47] Yuxiang Zhang, Odile Abraham, Alain Le Duff, Bertrand Lascoup, Vincent Tournat, Eric Larose, Thomas Planès, R. El Guerjouma, Olivier Durand, Monitoring the stress level of concrete structures with CODA wave interferometry: Experimental illustration of an investigated zone, in: *Proc. NDTMS 2011 Conf.*, ISBN: 978-94-007-0722-1, pp. 233–238, RILEM Bookseries 6.
- [48] Patrik Fröjd, Peter Ulriksen, Detecting damage events in concrete using diffuse ultrasound structural health monitoring during strong environmental variations, *Struct. Health Monit.* 17 (2) (2018) 410–419, <http://dx.doi.org/10.1177/1475921717699878>.
- [49] Patrik Fröjd, Peter Ulriksen, Continuous wave measurements in a network of transducers for structural health monitoring of a large concrete floor slab, *Struct. Health Monit.* 15 (4) (2016) 403–412, <http://dx.doi.org/10.1177/1475921716642139>.
- [50] Jean-Baptiste Legland, Yuxiang Zhang, Odile Abraham, Olivier Durand, Vincent Tournat, Evaluation of crack status in a meter-size concrete structure using the ultrasonic nonlinear coda wave interferometry, *J. Acoust. Soc. Am.* 142 (4) (2017) 2233–2241, <http://dx.doi.org/10.1121/1.5007832>.
- [51] Antoine Boniface, Jacqueline Saliba, Zoubir Mehdi Sbartai, Narintsoa Ranaivo-manana, Jean-Paul Balayssac, Evaluation of the acoustic emission 3D localisation accuracy for the mechanical damage monitoring in concrete, *Eng. Fract. Mech.* (ISSN: 0013-7944) 223 (2020) 106742, <http://dx.doi.org/10.1016/j.engfracmech.2019.106742>, URL: <https://www.sciencedirect.com/science/article/pii/S0013794419300499>.